



A numerical study of separation and stagnation points for steady and unsteady flow over an elliptic cylinder near a moving wall

Cite as: Phys. Fluids **33**, 083617 (2021); <https://doi.org/10.1063/5.0051740>

Submitted: 27 March 2021 • Accepted: 09 August 2021 • Published Online: 27 August 2021

 Jianxun Zhu (朱建勋) and  Lars Erik Holmedal



View Online



Export Citation



CrossMark

ARTICLES YOU MAY BE INTERESTED IN

[Experimental study on the development of wake vortices behind screen cylinders](#)

Physics of Fluids **33**, 085133 (2021); <https://doi.org/10.1063/5.0059089>

[Transition of wake flows past two circular or square cylinders in tandem](#)

Physics of Fluids **33**, 081705 (2021); <https://doi.org/10.1063/5.0062978>

[Stability of two-layer flows past slippery surfaces. I. Horizontal channels](#)

Physics of Fluids **33**, 084112 (2021); <https://doi.org/10.1063/5.0050256>

Celebrate **Open Access Week** With



LEARN MORE

A numerical study of separation and stagnation points for steady and unsteady flow over an elliptic cylinder near a moving wall

Cite as: Phys. Fluids **33**, 083617 (2021); doi: 10.1063/5.0051740

Submitted: 27 March 2021 · Accepted: 9 August 2021 ·

Published Online: 27 August 2021



View Online



Export Citation



CrossMark

Jianxun Zhu (朱建勋),^{a)}  and Lars Erik Holmedal 

AFFILIATIONS

Department of Marine Technology, Norwegian University of Science and Technology, 7052 Trondheim, Norway

^{a)} Author to whom correspondence should be addressed: jianxun.zhu@ntnu.no

ABSTRACT

Flow separation around an elliptic cylinder with an aspect ratio of 0.4 near a moving wall is investigated numerically for $Re \in [5, 150]$ with $G/D \in [0.1, 2]$ (where G denotes the distance between the cylinder bottom and the bottom wall, while D denotes the major-axis length of the cylinder). Four steady flow patterns are identified in $(Re, G/D)$ -space. A new flow pattern where only an anti-clockwise vortex is formed behind the lower part of the cylinder is observed for $G/D \geq 0.4$ with $Re \leq 24$. For steady flow, the upper separation point moves upstream as Re increases, while it is less affected by G/D . The lower separation point moves first downstream and then upstream as Re increases for $G/D \leq 0.4$, while for $G/D = 0.7$, only a large upstream movement is observed. The front stagnation point moves downstream toward the gap as Re decreases (for a given G/D) or as G/D decreases (for a given Re). The rear stagnation point moves first upward and then downward as Re increases for $G/D \leq 0.4$, while for $G/D = 0.7$, the opposite behavior is observed. For unsteady flow, the stagnation and separation points oscillate. Here, both the amplitude and the frequency decrease as G/D decreases. The oscillation amplitude for the lower separation point is slightly larger than for the upper separation point due to the stronger vortex shedding behind the cylinder bottom caused by the enhanced velocity through the gap. This mechanism also leads to larger oscillation amplitudes for both the front stagnation point and the lower separation point at larger G/D than for the isolated cylinder.

Published under an exclusive license by AIP Publishing. <https://doi.org/10.1063/5.0051740>

I. INTRODUCTION

Flow separation on a circular cylinder has been studied widely in the literature due to its fundamental importance for both academic research and engineering applications involving cylindrical structures in civil and ocean engineering.¹ Sumer and Fredsøe¹ found that for a circular cylinder, flow separation does not occur for Reynolds numbers (based on the cylinder diameter and the freestream velocity) smaller than 5. Wu *et al.*² and Sen *et al.*³ reported that the critical Reynolds number for the onset of the flow separation is between 6 and 7. They also found that as the Reynolds number increases up to approximately 46 (where the flow is steady without vortex shedding), the location of the flow separation on the upper and lower parts of the backside of the cylinder moves upstream along the cylinder, coinciding with the growth of the recirculation vortices attached to the cylinder. As the Reynolds number increases further, the location of the flow separation starts oscillating, as a result of the periodic vortex shedding behind the cylinder. Jiang⁴ found that the instantaneous

movement of the upper/lower separation points is governed by a dynamic balance between the upper/lower shear layers and the shear layer generated on the backside of the cylinder due to the wake recirculation. In the unsteady flow regime, the time-averaged location of the separation point moves upstream along the cylinder as the Reynolds number increases.⁴

Flow separation on a circular cylinder near a moving wall has been studied by Huang and Sung⁵ for Reynolds numbers ranging from 200 to 400 and by Jiang *et al.*⁶ for Reynolds numbers ranging from 35 to 300. The results (obtained from two-dimensional numerical simulations) show that as the gap ratio (defined by the ratio of the gap between the cylinder bottom and the moving wall to the cylinder diameter) decreases (for a given Reynolds number), the time-averaged location of the separation points both on the upper and lower parts of the cylinder moves upstream along the cylinder. Meanwhile, the time-averaged location of the front stagnation point moves downstream toward the gap along the cylinder. As the Reynolds number increases (for a given gap ratio), Jiang *et al.*⁶ found that the time-averaged

locations for the front stagnation point and the lower separation point move upstream, while for the upper separation point, it moves downstream along the cylinder.

Less attention has been paid to flow separation on elliptic cylinders although they are widely used as heat exchangers⁷ and bridge piers.⁸ In the steady flow regime, Paul *et al.*⁹ showed that the flow separation on an elliptic cylinder exhibits a qualitatively similar behavior at zero angle of attack (i.e., for flow direction parallel to the minor axis of the cylinder) as those for a circular cylinder. They also found that the critical Reynolds number for the onset of flow separation and vortex shedding decreases as the aspect ratio (AR) (the ratio between the minor- and major-axis lengths of the elliptic cylinder) decreases. Faruquee *et al.*¹⁰ and Sen *et al.*¹¹ obtained similar results. However, flow separation in the unsteady flow regime with periodic vortex shedding was not investigated in their work.

Flow around an elliptic cylinder with an aspect ratio of 0.4 near a moving wall has been investigated by Zhu *et al.*,¹² focusing on the wake patterns and hydrodynamic forces for Reynolds numbers ranging from 30 to 150 and gap ratios ranging from 0.1 to 5. This flow configuration is important for understanding the basic mechanisms for biological flows^{13,14} and for engineering applications such as low-speed underwater robots/vehicles with an elliptic cross section^{15,16} moving near seabed. However, the location of the separation and stagnation points for this flow configuration has not been studied systematically. This is the purpose of the present work, which is an extension of the work by Zhu *et al.*¹² In the present work, the near-wall effect on the stagnation and separation points for Reynolds numbers ranging from 5 to 150 and gap ratios ranging from 0.1 to 2 is investigated. The angle of attack is set to be 0°, and the aspect ratio of the cylinder is equal to 0.4. Four different flow patterns are found in the steady flow regime. Here, a new flow pattern, which is not presented in previous works,^{12,17} is identified, where only one anti-clockwise vortex exists behind the lower part of the cylinder. Moreover, a detailed analysis of the near-wall effect (i.e., the effect of the gap ratios) on the stagnation and separation points is presented for both the steady and the unsteady flow regimes.

II. PROBLEM DEFINITION AND GOVERNING EQS.

The sketch of an elliptic cylinder moving parallel to the wall at a constant velocity U_0 is shown in Figure 1, which also depicts the aspect ratio (AR) of the cylinder given by the minor (a) divided on major (D) axis length and the gap ratio (G/D), where G is the gap between the cylinder bottom and the moving wall.

In the present work, a uniformly translating frame of referenced fixed on the cylinder is used to make it convenient for the numerical simulations. Hence, the cylinder is stationary, while the wall and the fluid move toward the right at a constant speed U_0 . The Reynolds number is based on the major axis, i.e., $Re = U_0 D / \nu$, where ν is the kinematic viscosity. Here, the incompressible flow with a constant density ρ is governed by the following dimensionless two-dimensional Navier–Stokes equations:

$$\frac{\partial u_i}{\partial x_i} = 0, \tag{1}$$

$$\frac{\partial u_i}{\partial t} + \frac{\partial u_i u_j}{\partial x_j} = -\frac{\partial p}{\partial x_i} + \frac{1}{Re} \frac{\partial^2 u_i}{\partial x_j \partial x_j}, \tag{2}$$

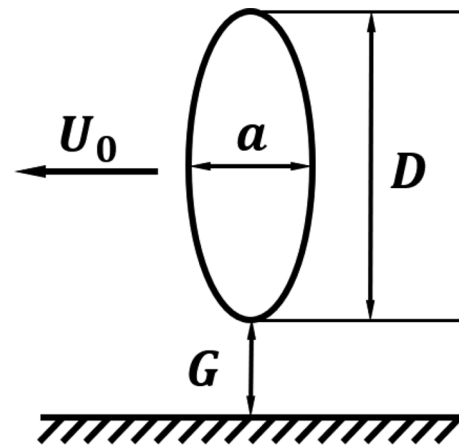


FIG. 1. Sketch of the elliptic cylinder moving parallel to a wall at a constant velocity U_0 .

where the Einstein notation using repeated indices is applied. Here, $u_i = (u, v)$ and $x_i = (x, y)$ for $i = 1$ and 2 indicate the velocity and Cartesian coordinates, respectively, while t and p denote the time and pressure, respectively. The velocity, time, pressure, and length are scaled by $U_0, D/U_0, \rho U_0^2$, and D , respectively.

III. NUMERICAL METHODS

A projection method is used for solving equations (1) and (2). The convective terms and the diffusive terms are discretized by Adams–Bashforth and Crank–Nicolson schemes, respectively. The spatial derivatives are discretized with a second-order centered finite difference scheme on a staggered grid arrangement. The Poisson equation for pressure correction is solved using a biconjugate gradient stabilized method (BiCGSTAB) with a SIP (Strongly Implicit Procedure; Stone’s method) preconditioner. The cylinder geometry is taken into account by a direct-forcing immersed boundary method. More details about this method were given by Zhu *et al.*¹²

IV. VALIDATION AGAINST PREVIOUS NUMERICAL RESULTS

The present numerical method has been validated in a previous work¹² for flow around an isolated circular cylinder for $Re = 40, 100$, and 200. In the present work, two-dimensional numerical simulations for flow around an isolated circular cylinder are conducted for $Re \in [10, 40]$ to investigate the angular position of the flow separation point on the cylinder surface. A dimensionless free-stream velocity $U_0 = 1$ is specified at the inlet boundary, while a Neumann condition is imposed for the velocity at the outlet and at the lateral boundaries. A no-slip condition is applied at the cylinder. The pressure is set to be zero at the outlet, and a Neumann condition for the pressure correction is imposed at the other boundaries.

The top, bottom, and inlet boundaries are located 10 cylinder diameters away from the cylinder center, while the outlet is located 20 cylinder diameters downstream of the cylinder center. Here, the blockage B (the distance between the cylinder top and the top of the computational domain divided on the cylinder radius; this is the same here as the distance between the cylinder bottom and the bottom of the computational domain, divided on the cylinder radius) equals to 0.05,

which is small enough to obtain domain independent results as previously shown by Sen *et al.*³ A uniform grid ($\Delta x = \Delta y = 0.01$) is applied in a small square region around the cylinder (i.e., $-0.7 \leq x \leq 0.7$ and $-0.7 \leq y \leq 0.7$). From the edges of this region, the grid is stretched (using geometric series) in both the horizontal and vertical directions using stretch ratios less than 1.05.

Figure 2(a) shows the streamline of the flow around an isolated circular cylinder for $Re = 30$ to illustrate the upper (U) and lower (L) separation points as well as the front (F) and rear (R) stagnation points on the cylinder surface. The positions of these four critical points are identified by the vanishing of the shear stress on the cylinder surface. Here, the angular position (θ) is measured anti-clockwise from the center point on the backside of the cylinder. It ranges from 0° to 180°

and from 0° to -180° along the top half and the bottom half of the cylinder, respectively. Figure 2(b) shows the angular position (θ_U) of the upper separation point for $Re \in [10, 40]$. A linear relationship between θ_U and $Re^{-0.5}$ is observed, showing good agreement with previous numerical results of the upper separation angle θ_U obtained by Sen *et al.*³ and Takami and Keller¹⁸ for $B = 0.05$ and 0.059 , respectively. Figures 2(c) and 2(d) show the distribution of the pressure coefficient C_p and the vorticity $\omega = \partial v / \partial x - \partial u / \partial y$, respectively, along the bottom half of the cylinder for $Re = 40$. Here, C_p is defined by $(p - p_\infty) / (0.5 \rho U_0^2)$, where p_∞ is the pressure at the outlet and U_0 is the inlet velocity. These results are in good agreement with the numerical results obtained by Sen *et al.*³ for C_p and Dennis and Chang¹⁹ as well as Tseng and Ferziger²⁰ for ω . Furthermore, a validation study is

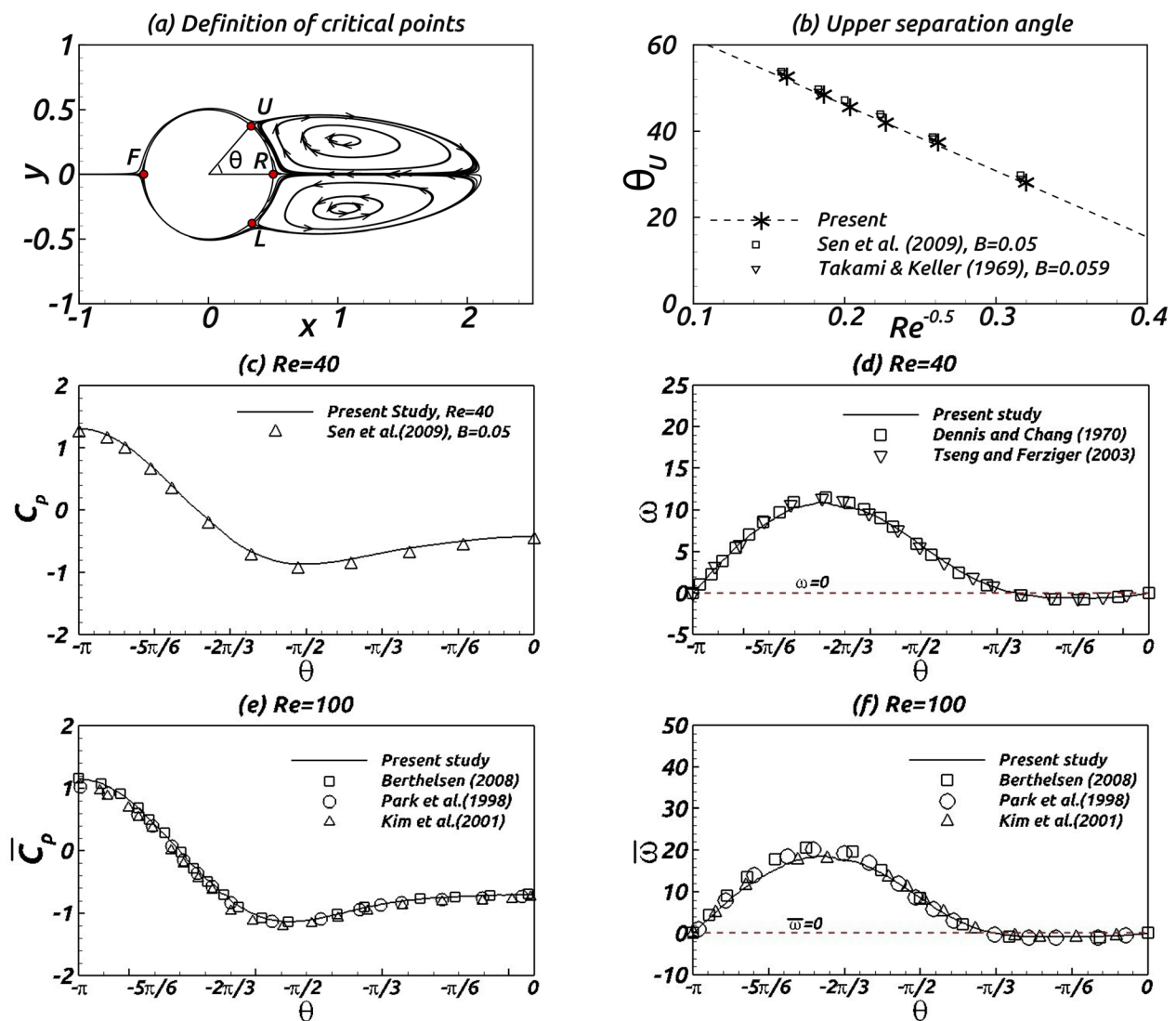


FIG. 2. (a) Sketch of the upper (U) and lower (L) separation points as well as the front (F) and rear (R) stagnation points using the streamline for flow around an isolated circular cylinder for $Re = 30$; (b) variation of the separation angle θ_U with $Re^{-0.5}$ for steady flow around an isolated cylinder for $Re \in [10, 40]$; (c)-(f) distribution of the (time-averaged) pressure coefficient (c and e) and the (time-averaged) vorticity (d and f) distribution on the bottom half of the cylinder for $Re = 40$ and 100 .

TABLE I. Comparison of $\overline{C_D}$ and St with previous numerical results^{24,25} for flow around an isolated elliptic cylinder with $AR = 0.5$ for $Re = 150$.

$AR = 0.5, Re = 150$	$\overline{C_D}$	St
Thompson <i>et al.</i> ²⁵	1.78	0.189
Shi <i>et al.</i> ²⁴	1.82	0.191
Present	1.81	0.195

conducted for $Re = 100$, where vortex shedding behind the circular cylinder is present. A good agreement with previous numerical results of Berthelsen and Faltinsen,²¹ Kim *et al.*,²² and Park *et al.*²³ is obtained for both the time-averaged pressure coefficient $\overline{C_p}$ and the time-averaged vorticity $\overline{\omega}$ along the bottom half of the cylinder, as shown in Figs. 2(e) and 2(f), respectively. Here, 40 vortex-shedding cycles are included for obtaining the time-averaged values. It should be noted that the pressure coefficient at the front stagnation point is larger than 1, i.e., $(p_s - p_\infty)/(0.5\rho U_0^2) > 1$, where p_s is the stagnation pressure. Based on the Bernoulli equation along a streamline from the inlet to the front stagnation point, the value of $(p_s - p_{in})/(0.5\rho U_0^2)$ (where p_{in} is the pressure at the inlet) is equal to 1. The drag of the cylinder induced by the fluid viscosity leads to p_{in} being larger than p_∞ , thus $(p_s - p_\infty)/(0.5\rho U_0^2) > 1$.

A simulation for flow around an isolated elliptic cylinder with $AR = 0.5$ has been conducted for $Re = 150$. Here, the computational domain is same as that of Shi *et al.*²⁴ The top, bottom, and inlet boundaries are located $50D$ away from the cylinder center, while the outlet is located $100D$ downstream of the cylinder center. Table I lists the time-averaged drag coefficient [$\overline{C_D} = 2F_D/(\rho U_0^2 DT)$, where T denotes 200 time units] and the Strouhal number ($St = fD/U_0$, where f is the vortex shedding frequency). The present results are in good agreement with the numerical results obtained by Shi *et al.*²⁴ and in reasonable agreement with the numerical results obtained by Thompson *et al.*²⁵

V. RESULTS AND DISCUSSION

Numerical investigations of flow around an elliptic cylinder with an aspect ratio $AR = 0.4$ near a moving wall have been conducted for Re ranging from 5 to 150 for gap ratios G/D ranging from 0.1 to 0.7. Figure 3 shows the computational domain, the location of the cylinder,

TABLE II. Comparisons of the $\overline{\theta}_U$, $\overline{\theta}_L$, $\overline{\theta}_F$, and $\overline{\theta}_R$ (given by degrees) obtained by the computation domain with the “Coarse,” Medium, and Fine grid resolutions as well as the Fine grid resolution with a refined grid resolution in the wake (Refine wake) for flow around an elliptic cylinder near a moving wall at $Re = 150$ with $G/D = 0.1$.

Mesh ($G/D = 0.1$)	$\overline{\theta}_U$ (°)	$\overline{\theta}_L$ (°)	$\overline{\theta}_F$ (°)	$\overline{\theta}_R$ (°)
Coarse ($\Delta x = \Delta y = 0.02$)	85.0	-75.1	-111.0	41.3
Medium ($\Delta x = \Delta y = 0.015$)	85.7	-76.3	-111.4	41.9
Fine ($\Delta x = \Delta y = 0.01$)	86.3	-77.1	-111.7	42.1
Refine wake ($\Delta x = \Delta y = 0.01$)	86.3	-77.1	-111.7	41.7

and the boundary conditions. The inlet and top boundaries are located $20D$ away from the cylinder center, the outlet is located $40D$ downstream of the cylinder center, and the bottom boundary is located $(G/D + 0.5)D$ from the cylinder center. A constant dimensionless velocity $U_0 = 1$ is set at the inlet, and a Neumann condition is imposed for the velocity at the top and outlet boundaries. A no-slip condition is applied at the cylinder and the bottom wall, which moves toward the right at $U_0 = 1$. The pressure is equal to zero at the outlet, and a Neumann condition for the pressure correction is imposed at the other boundaries.

A uniform grid (i.e., $\Delta x = \Delta y$) is applied to a region (marked by a blue rectangle in Fig. 3) around the cylinder. The top, left, and right edges of this region are located $0.7D$ away from the cylinder center, and the bottom edge is located $(0.5D + G)$. The grid is stretched from the top, left, and right edges toward the top, inlet, and outlet boundaries using constant stretch ratios less than 1.05.

To test grid independence, numerical simulations were conducted using four different grid resolutions. Table II shows the time-averaged angular positions of the upper ($\overline{\theta}_U$) and lower ($\overline{\theta}_L$) separation points as well as the front ($\overline{\theta}_F$) and rear ($\overline{\theta}_R$) stagnation points for $Re = 150$ and $G/D = 0.1$, where the strongest wall effect was present. The results obtained from the “Fine” grid (see Table II) deviate between 0.2° and 0.8° from those obtained from the “Medium” grid. The value of $\overline{\theta}_R$ obtained from the “Refine wake” grid (where the grid resolution in the wake is 1.5 times finer than the Fine grid) deviates 0.4° from that obtained from the Fine grid, while $\overline{\theta}_U$, $\overline{\theta}_L$, and $\overline{\theta}_F$ remain the same. Figure 4 shows the time-averaged pressure

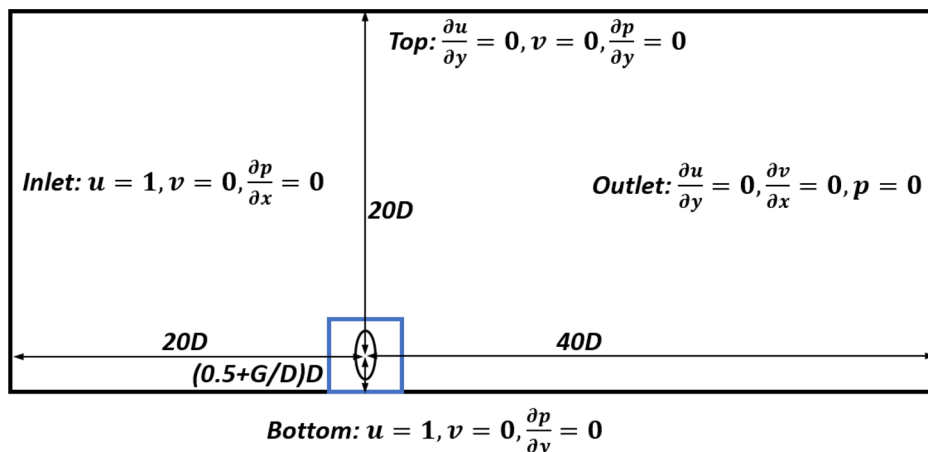


FIG. 3. Sketch of the computational domain and boundary conditions for flow around an elliptic cylinder near a moving wall.

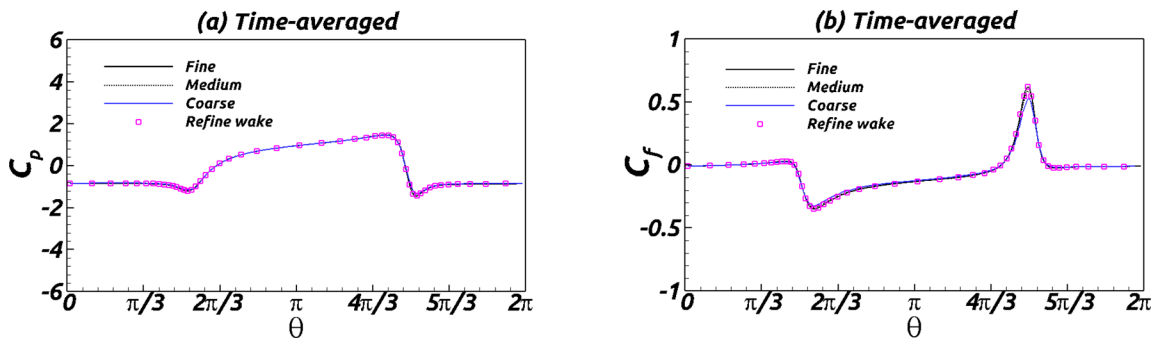


FIG. 4. (a) Time-averaged pressure ($\overline{C_p}$) and (b) skin friction ($\overline{C_f}$) coefficients obtained from four different grid resolutions for flow around the cylinder near a moving wall at $G/D = 0.1$ for $Re = 150$. Here, θ is measured anti-clockwise from the center point on the cylinder back.

coefficient ($\overline{C_p} = C_p/T$, where T denotes 400 time units) and the time-averaged skin friction coefficient [$\overline{C_f} = \tau_w / (0.5\rho U_0^2 T)$, where τ_w is the wall shear stress] around the elliptic cylinder. A good grid convergence is obtained for these two coefficients.

Table III shows the time-averaged, maximum, and minimum values of θ_U , θ_L , θ_F , and θ_R for $Re = 150$ and $G/D = 2.0$, where the flow separation is weakly affected by the moving wall. The results obtained from the Fine grid deviate less than 0.7° and 0.3° from the Medium and Refine wake grids, respectively. Moreover, a good grid convergence for C_p and C_f is obtained for the time-averaged values [Figs. 5(a) and 5(b)] and for the maximum value of C_l [Figs. 5(c) and 5(d)] as well as the minimum value of C_l [Figs. 5(e) and 5(f)]. In the present study, the Fine grid (see Tables II and III) is used to obtain the grid independent results.

A. Steady flow pattern

Figure 6 shows the streamlines for flow around the elliptic cylinder near a moving wall for $G/D = 0.4$ and $Re \in [7, 30]$. For $Re = 7$ [Fig. 6(a)], only a clockwise (upper) vortex is formed behind the upper part of the cylinder. This flow is denoted as the “upper-vortex” flow pattern. As Re increases to 8 [Fig. 6(b)], the upper vortex grows, while an anti-clockwise lower vortex is formed due to an increase in vorticity convecting into the wake as the flow passes beneath the cylinder bottom with an increased velocity.^{12,25} This flow is denoted as the “two-vortices” flow pattern. As Re increases to 10 [Fig. 6(c)], the upper vortex core moves downstream. As Re increases further to 13

[Fig. 6(d)], the upper vortex moves further downstream while decaying and, finally, disappears for $Re = 20$ [Fig. 6(e)] due to the downstream vorticity dissipation, which is further visualized by the vorticity contours (red lines) and the streamlines (black lines) in Figs. 7(a) and 7(b) for $Re = 10$ and 13, respectively. This flow is denoted as the “lower-vortex” flow pattern. As Re increases to 27 [Fig. 6(f)], the upper vortex re-appears and grows together with the lower vortex as Re increases further to 30 [Fig. 6(g)]. It appears that the weakening of the upper vortex caused by the downstream vorticity dissipation is compensated by the increase in vorticity convecting into the wake as Re increases.

Figure 8 shows the different flow patterns in the $(G/D, Re)$ -space. For $G/D = 0.4$, the flow exhibits a transition sequence of upper-vortex \rightarrow two-vortices \rightarrow lower-vortex \rightarrow two-vortices flow patterns as Re increases as visualized in Fig. 6. As G/D increases to 0.5, this transition sequence persists but with a smaller critical Re for the transition between two different flow patterns. The decrease in the critical Re for the transition from the upper-vortex to two-vortices flow pattern as G/D increases is due to the weakening of the wall suppression effect. The decrease in the critical Re for the transition from two-vortices to lower-vortex flow pattern as G/D increases is due to the decrease in the velocity over the cylinder top [Fig. 9(a)] and less circulation ($\Gamma = -\int_{G/D+1}^2 u\omega_z dy$) convecting into the wake [Fig. 9(b)] for $Re = 30$ and for $G/D \in [0.4, 0.7]$. Zhu *et al.*¹² found that as G/D increases, the upper vortex core moves upstream. This behavior weakens the downstream vorticity dissipation of the upper vortex, which explains the decrease in the critical Re for the formation of the upper vortex, i.e., the transition from the lower-vortex to the two-vortices

TABLE III. Comparisons of the maximum, minimum, and mean values of θ_U , θ_L , θ_F , and θ_R (given by degrees) obtained by the computation domain with the Coarse, Medium, and Fine grid resolutions as well as the Fine grid resolution with a refined grid resolution in the wake (Refine wake) for flow around an elliptic cylinder near a moving wall at $Re = 150$ with $G/D = 2$.

Mesh ($G/D = 2$)	θ_U ($^\circ$)			θ_L ($^\circ$)			θ_F ($^\circ$)			θ_R ($^\circ$)		
	Max.	Min.	Mean	Max.	Min.	Mean	Max.	Min.	Mean	Max.	Min.	Mean
Coarse	83.6	79.6	81.6	-158.9	-186.0	-172.3	-79.2	-82.9	-81.2	76.7	-74.7	2.1
Medium	84.3	80.9	82.7	-159.7	-186.4	-172.9	-80.2	-83.6	-81.8	76.7	-74.4	2.2
Fine	84.8	81.6	83.3	-159.7	-186.7	-172.7	-80.9	-84.2	-82.6	76.4	-74.5	2.1
Refine wake	84.8	81.6	83.3	-159.6	-186.4	-172.6	-80.9	-84.2	-82.6	76.4	-74.4	2.0

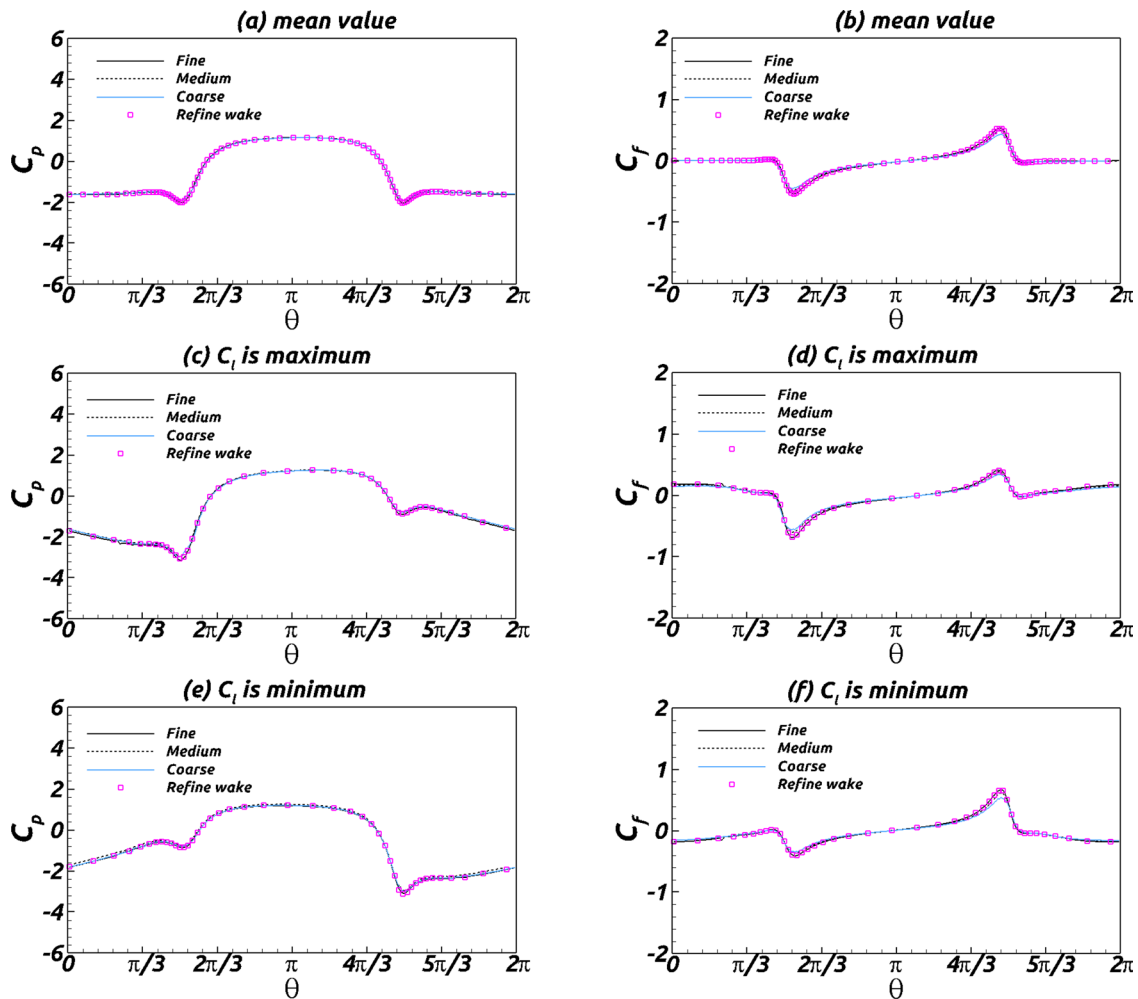


FIG. 5. The pressure ($\overline{C_p}$) and skin friction ($\overline{C_f}$) coefficients for the time-averaged values [(a) and (b)] and for the maximum value of C_l [(c) and (d)] as well as the minimum value of C_l [(e) and (f)] obtained from four different grid resolutions for flow around the cylinder near a moving wall at $G/D = 2.0$ for $Re = 150$. Here, θ is measured anti-clockwise from the center point on the cylinder back.

flow pattern as G/D increases. Furthermore, the decrease in the critical Re for the transition between different flow patterns persists as G/D increases up to 0.7. As a result, the upper-vortex flow pattern does not occur for $G/D \geq 0.6$ with $Re \in [5, 60]$.

For $G/D \leq 0.3$, the flow exhibits a transition sequence of “no-separation” \rightarrow upper-vortex \rightarrow two-vortex flow patterns as Re increases. Here, the lower-vortex flow pattern is not present. This can be explained by that a decrease in G/D leads to more fluid being transported toward the top of the cylinder,¹² resulting in more vorticity being convected into the wake over the cylinder top, thus forming a stronger upper vortex. This counteracts the downstream vorticity dissipation, thus preventing the disappearance of the upper vortex, i.e., the onset of the lower-vortex flow pattern. Moreover, as G/D decreases to 0.1, the critical Re for the transition from upper-vortex to two-vortex flow pattern increases. This is because a larger Re is required to form the lower vortex when the wall suppression effect becomes stronger.

B. Separation and stagnation angle

1. Steady flow

Figure 10 shows the angular position of the upper separation point θ_U , the front stagnation point θ_F , the lower separation point θ_L , and the rear stagnation point θ_R , for flow around the elliptic cylinder near a moving wall with $G/D \in [0.1, 0.7]$ and $Re \in [5, 110]$. As a reference, numerical simulations for flow around an isolated elliptic cylinder with $AR = 0.4$ are also conducted for $Re \in [10, 30]$. The predictions of θ_U and θ_L for this configuration are plotted in Figs. 10(a) and 10(c), respectively. The values of θ_F and θ_R for the isolated cylinder are equal to -180° and 0° , respectively. Here, the flow is in the steady state without vortex shedding.

The upper separation point [Fig. 10(a)] both for the isolated cylinder and the near-wall cylinder moves upstream along the backside of the cylinder as Re increases (for a given G/D). The presence of the wall leads to the upper separation point moving

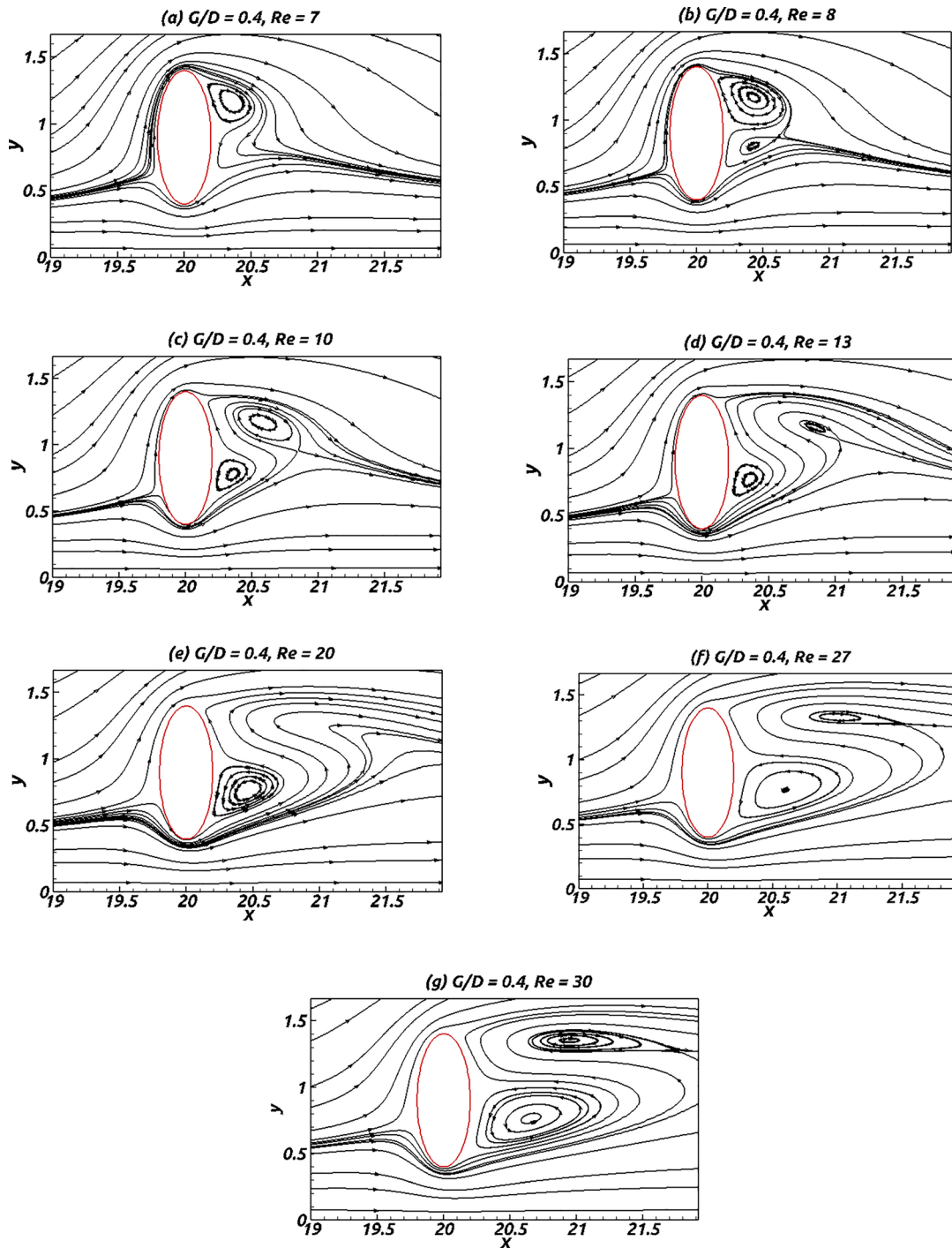


FIG. 6. Streamlines for the flow around an elliptical cylinder near a moving wall for $G/D = 0.4$ with $Re =$ (a) 7, (b) 8, (c) 10, (d) 13, (e) 20, (f) 27, and (g) 30.

upstream along the backside of the cylinder due to the blockage effect in the gap. For the near-wall cylinder, a large increase in θ_U is observed as Re increases from 5 to 20. This behavior is consistent with the large downstream movement of the upper vortex core

with increasing Re as shown in Figs. 6(a) and 6(d). As Re increases further, the variation of θ_U with Re becomes smaller, which is consistent with the small movement of the upper vortex core, as shown in Figs. 6(f) and 6(g).

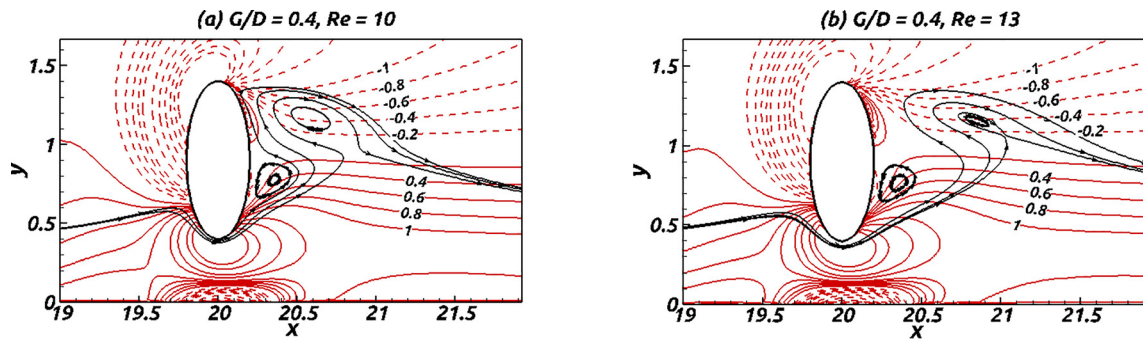


FIG. 7. Streamlines (black line) and vorticity contours (red line) for the flow around a near-wall elliptical cylinder with $AOA = 0^\circ$ for $G/D = 0.4$ for (a) $Re = 10$ and (b) $Re = 13$.

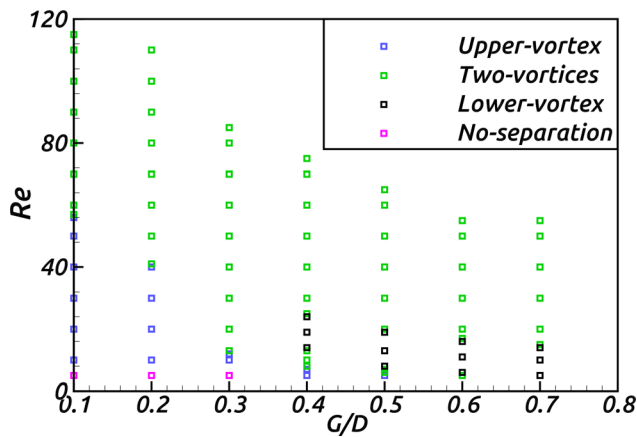


FIG. 8. Distribution of different flow patterns in $(G/D, Re)$ -space.

The front stagnation point [Fig. 10(b)] moves upstream along the cylinder as Re increases (for a given G/D) or as G/D increases (for a given Re). A qualitatively similar behavior has been observed previously for flow around a circular cylinder near a moving wall.⁶ Moreover, as G/D decreases, the effect of Re on θ_F becomes weaker; this is because of the strong blockage effect for small G/D and the resulting suppression of the gap flow, which counteracts the upward movement of the front stagnation point as Re increases.

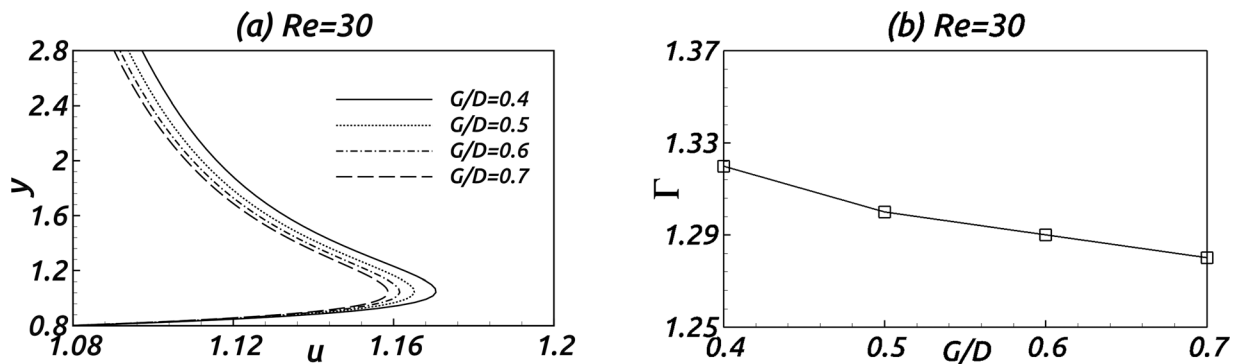


FIG. 9. (a) Streamwise velocity profile u along the vertical centerline above the cylinder for $Re = 30$ with different G/D and (b) the circulation Γ connecting into the wake over the cylinder top.

The lower separation point both for the near-wall cylinder at $G/D = 0.7$ and for the isolated cylinder [Fig. 10(c)] moves downstream along the backside of the cylinder as Re increases, which is consistent with the growth of the lower vortex. For $G/D = 0.4$, an increase in Re up to 8 leads to an increase in the gap flow velocity, resulting in the lower separation point moving downstream along the backside of the cylinder. As Re increases further, this point moves downstream along the cylinder, coinciding with the growth of the lower vortex as visualized in Figs. 6(c)–6(h). A qualitatively similar behavior is observed for $G/D = 0.1$ and 0.2 . However, the effect of Re on the location of the lower separation point is weaker here. It should be noted that the lower separation point for the isolated cylinder is located farther upstream along the cylinder than for the near-wall cylinder due to the blockage effect. An exception is observed for $G/D = 0.1$ and $Re = 10$; here, the large gap flow velocity outweighs the blockage effect.

For $G/D \in [0.1, 0.4]$, the rear stagnation point [Fig. 10(d)] moves downstream along the backside of the cylinder as Re increases. This is mainly induced by the growth of the upper vortex as shown in Figs. 6(a)–6(c) for $G/D = 0.4$. As Re increases further, the upper vortex detaches from the cylinder, while the lower vortex grows [Figs. 6(d)–6(h)], resulting in the rear stagnation point moving upward along the backside of the cylinder [Fig. 10(d)]. It should also be noted that as G/D decreases from 0.4 to 0.1 , this upward movement becomes smaller due to the weakening of the lower vortex caused by the wall suppression effect. For $G/D = 0.7$, the rear stagnation point moves upward along the backside of the cylinder as Re increases up to 20,

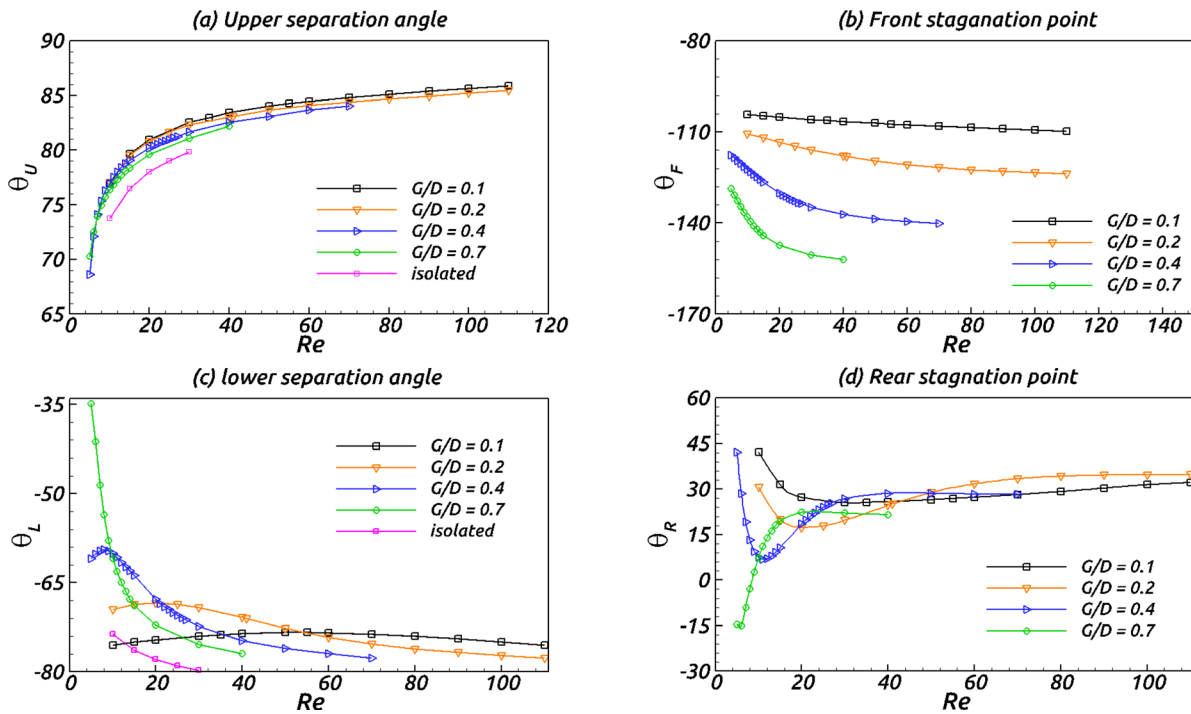


FIG. 10. The angular position of (a) the upper separation point θ_U , (b) the front stagnation point θ_F , (c) the lower separation point θ_L , and (d) the rear stagnation point θ_R for the near-wall cylinder with $G/D = 0.1, 0.2, 0.4,$ and 0.7 at $Re \in [5, 110]$ as well as for the isolated cylinder with $Re \in [10, 30]$.

coinciding with the growth of the lower vortex. As Re increases further, the growth of the upper vortex leads to the rear stagnation point moving downward along the backside of the cylinder.

2. Unsteady flow

Numerical simulations of flow around an elliptic cylinder near a moving wall are conducted for $Re = 150$ with $G/D \in [0.1, 2.0]$. Here, vortex shedding occurs behind the cylinder, resulting in a time-dependent position of the separation and stagnation points on the cylinder. As a reference, a numerical simulation for flow around an isolated elliptic cylinder with $AR = 0.4$ is also conducted for $Re = 150$.

Jiang⁴ investigated the separation angle for flow past a circular cylinder in the subcritical regime using both 2D and 3D simulations. He found that the flow three-dimensionality is dominated by large-scale 3D structures (mode A) farther down in the wake, which has a small impact on the separation angle. However, the amount of disorderly small-scale 3D structures (mode B) in the vicinity of the cylinder (which might have a large impact on the separation angle) increases as the Reynolds number increases. Jiang⁴ found that for flows dominated by large-scale 3D structures, the time- and span-averaged separation angles obtained from the 3D simulations only deviate approximately 1% from the corresponding separation angle obtained from 2D simulations. Experimental results of Radi *et al.*²⁶ showed that for $100 < Re < 220$, the flow around an isolated elliptic cylinder with $AR = 0.39$ exhibits 3D flow instability with large 3D structures (i.e., larger than the mode A structure for the circular cylinder). Numerical results obtained by Zhu *et al.*²⁷ for the flow around an elliptic cylinder

with $AR = 0.5$ near a moving wall showed that the disorderly small-scale 3D structures in the vicinity of the cylinder do not occur for $Re < 200$ for $G/D \in [0.1, 0.4]$. Based on these investigations, it is expected that the present 2D simulation will give reasonably accurate results for the separation and stagnation angles on the cylinder, which is the primary focus of this paper.

Figure 11 shows the time-history of (a) θ_U , (b) θ_F , (c) θ_L , and (d) θ_R for $G/D = 0.1, 0.4,$ and 0.7 and for the isolated cylinder at $Re = 150$. For $G/D = 0.1$, the front stagnation point (θ_F) and the upper (θ_U) and lower (θ_L) separation points remain nearly stationary while the rear stagnation point (θ_R) oscillates on the backside of the cylinder. This can be further visualized by vorticity contours and instantaneous streamlines (solid lines with arrows) as shown in Fig. 12, where A, B, C, and D represent the instants shown in Fig. 11(d). From the instants A and B [Figs. 12(a) and 12(b)], the upper shear layer with negative vorticity separates from the cylinder top. The resulting upper vortex in the wake induces a recirculation flow (see the instantaneous streamlines) moving upward along the backside of the cylinder, leading to the growth of the shear layer P with positive vorticity. This results in a downward movement of the rear stagnation point (R) along the cylinder, which is consistent with the decrease in θ_R from A to B, as shown in Fig. 11(d). From the instants C and D [Figs. 12(c) and 12(d)], the lower shear layer with positive vorticity separates from the cylinder bottom. The resulting lower vortex induces a recirculation flow moving downward along the backside of the cylinder, leading to the growth of the shear layer Q with negative vorticity. This causes an upward movement of the rear stagnation point, coinciding with the increase in θ_R from C to D, as shown in Fig. 11(d). Moreover, the

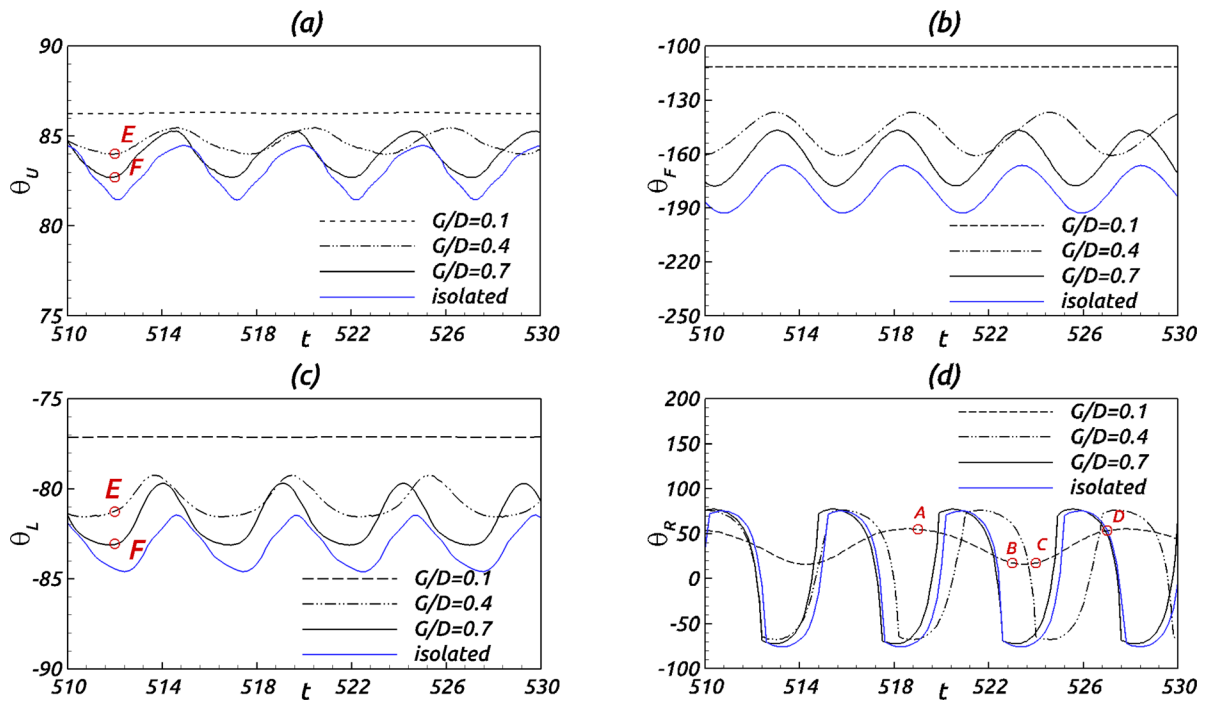


FIG. 11. Time history of (a) the upper separation point θ_U , (b) the front stagnation point θ_F , (c) the lower stagnation point θ_L , and (d) the rear stagnation point θ_R for flow separation and stagnation points around the isolated cylinder and the near-wall cylinder with $G/D = 0.1, 0.4$, and 0.7 at $Re = 150$.

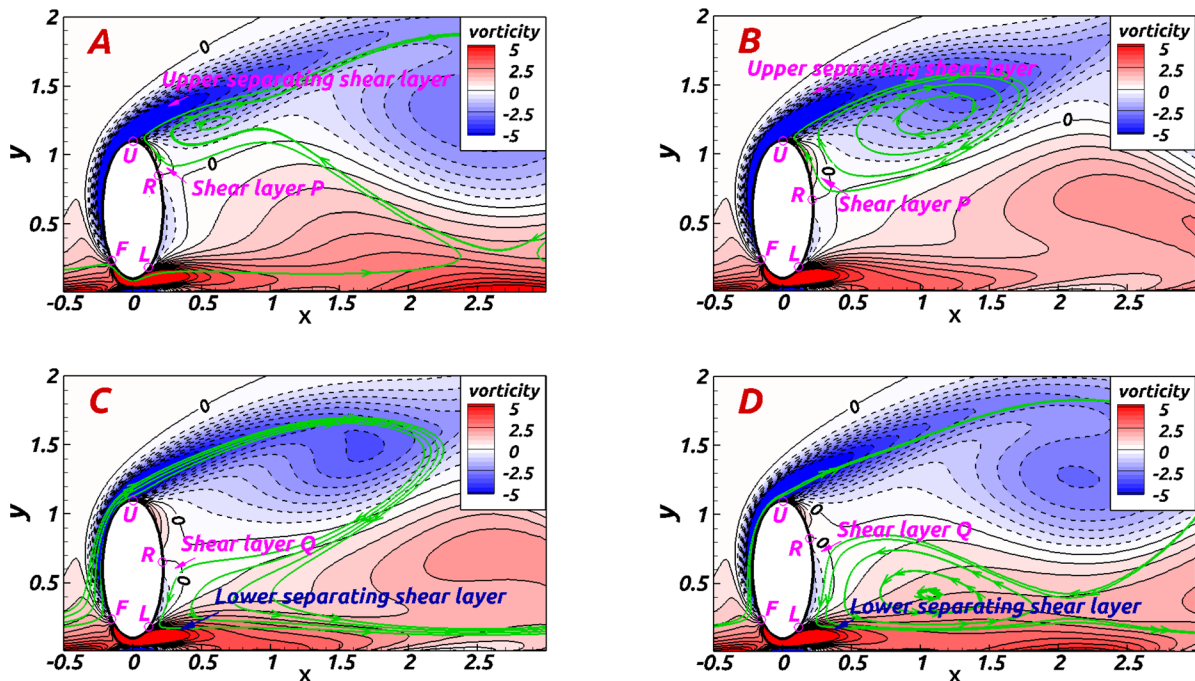


FIG. 12. Vorticity contours for the flow around the cylinder near a moving wall at $G/D = 0.1$ for $Re = 150$ at instants (a), (b), (c), and (d); solid and dashed lines indicate the positive and negative values, respectively, while solid lines with arrows denote the instantaneous streamlines.

position for the other three critical points remains nearly the same from instants *A* to *D*, which is consistent with the constant values of θ_U , θ_F , and θ_L for $G/D = 0.1$ [Figs. 11(a)–11(c)].

For $G/D = 0.4$ and 0.7 , both the separation and stagnation points exhibit oscillation (Fig. 11). Moreover, the oscillation frequency of these four points increases as G/D increases due to the weakening of the wall suppression effect. It should also be noted that for θ_L [Fig. 11(c)], the trough of the curve is wider, while the crest is sharper due to the wall suppression effect. This can be further visualized by the vorticity contours shown in Fig. 13 for $G/D = 0.4$ and 0.7 at instants *E* and *F* [Fig. 11(c)], showing the interaction between the lower vortex with positive vorticity and the bottom-wall shear layer with negative vorticity.

For the isolated cylinder, the troughs of the curves for both θ_U and θ_L [Figs. 11(a) and 11(c)] become sharper than those for the near-wall cylinder due to the absence of the wall suppression effect on the upper separation point. The time variation of θ_F [Fig. 11(b)] for the isolated cylinder is similar to that for $G/D = 0.7$ but with smaller values due to the absence of the blockage effect in the gap. The time variation of θ_R [Fig. 11(d)], which is dominated by the dynamic balance between the shear layers on the backside of the cylinder and the upper and lower shear layers (Fig. 12), is almost same as that for $G/D = 0.7$.

Figure 14 shows the range of values of (a) θ_U , (b) θ_F , (c) θ_L , and (d) θ_R for $G/D \in [0.1, 2.0]$ and for the isolated cylinder at $Re = 150$. The oscillation amplitudes for θ_U and θ_R (given by the distance between the maximum and minimum values for a given G/D) increase toward the values obtained for the isolated cylinder due to the weakening of the wall suppression effect as G/D increases. Furthermore, the oscillation amplitudes for θ_F and θ_L first increase up to their maximum values; then, they decrease toward the values obtained for the isolated cylinder as G/D increases. It should be noted that the values for the isolated cylinder are exceeded for $G/D \in [0.5, 2]$ (for θ_F) and for $G/D \in [0.6, 2]$ (for θ_L). This is because an enhanced gap flow velocity here induces a stronger vortex shedding behind the cylinder bottom, counteracting the wall suppression effect.

The oscillation amplitude is largest for the rear stagnation point because of the significant growth and decay of the shear layers *Q* and *P* during the vortex shedding as visualized in Fig. 12. It appears that the oscillation amplitude is smaller for the upper separation point than for the lower separation point. This is because a decrease in G/D leads to an increase in the gap flow velocity, resulting in a stronger vortex

shedding from the cylinder bottom and, hence, an increase in the oscillation amplitude of the lower separation point. Moreover, the value of G/D affects the minimum values more than the maximum values (Fig. 14). This is because the stagnation and separation points exhibit a stronger interaction with the bottom wall when they move downward along the cylinder (i.e., as they approach the minimum value).

VI. SUMMARY AND CONCLUSIONS

In this work, the flow around an elliptic cylinder near a moving wall has been investigated for Reynolds numbers ranging from 5 to 150 and for gap ratios ranging from 0.1 to 0.7. The flow separation both in the steady and unsteady flow regimes has been investigated.

For steady flow, four different flow patterns have been identified: (i) the no-separation flow pattern where flow separation does not occur; (ii) the two-vortices flow pattern where two counter-rotating recirculation vortices are formed behind the cylinder; (iii) the upper-vortex flow pattern where only one clockwise vortex is formed behind the top part of the cylinder; and (iv) the lower-vortex flow pattern where only one anti-clockwise vortex is formed behind the lower part of the cylinder.

For gap ratios ranging from 0.4 to 0.7, the flow exhibits a transition sequence of upper-vortex \rightarrow two-vortices \rightarrow lower-vortex \rightarrow two-vortices flow patterns as the Reynolds number increases. The critical Reynolds number for the transition between two different flow patterns decreases as the gap ratio increases, such that the upper-vortex and the two-vortices flow patterns are not present for gap ratios larger than 0.5 and 0.6, respectively. For gap ratios smaller than 0.4, the lower-vortex flow pattern is not present, such that the flow exhibits a transition sequence of no-separation \rightarrow upper-vortex \rightarrow two-vortex flow patterns as the Reynolds number increases.

The upper separation point moves upstream along the backside of the cylinder as the Reynolds number increases (for a given gap ratio), while it is only weakly affected by the gap ratio (for a given Reynolds number). The front stagnation point moves upstream along the cylinder as the Reynolds number increases (for a given gap ratio) or as the gap ratio increases (for a given Reynolds number). Moreover, a decrease in the gap ratio leads to a smaller change of the front stagnation point location as the Reynolds number increases due to the stronger blockage effect in the gap.

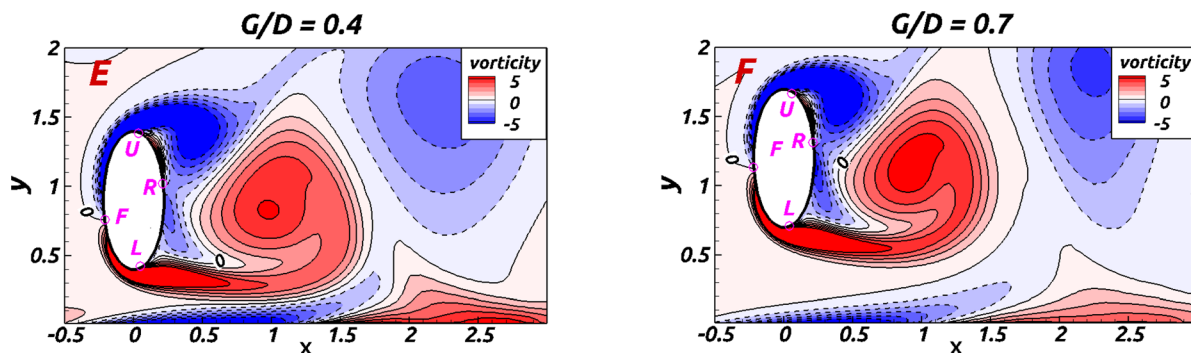


FIG. 13. Instantaneous vorticity contours for the flow around the cylinder near a moving wall at $G/D = 0.4$ (left) and 0.7 (right) for $Re = 150$; solid and dashed lines indicate the positive and negative values of the vorticity, respectively.

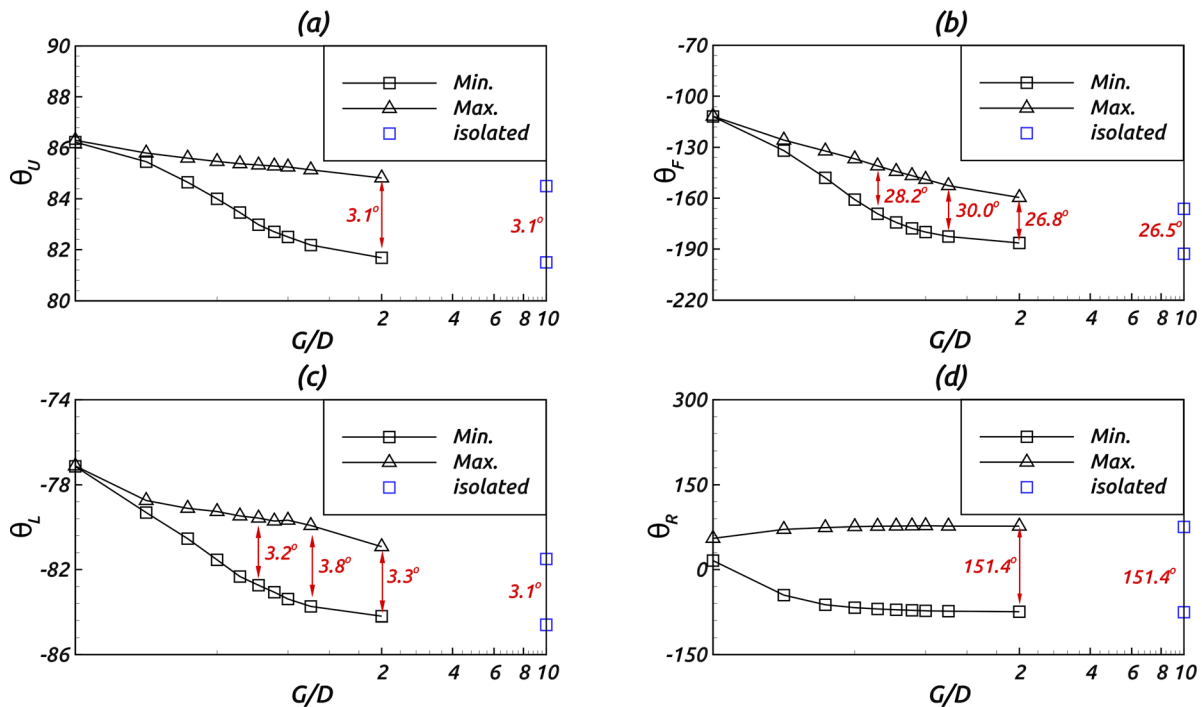


FIG. 14. Maximum and minimum values of (a) θ_U , (b) θ_F , (c) θ_L , and (d) θ_R for the isolated cylinder and for the near-wall cylinder with $G/D \in [0.1, 2]$ at $Re = 150$. Red numbers represent the difference between the minimum and maximum values.

The lower separation point moves first downstream and then upstream along the backside of the cylinder as the Reynolds number increases at small gap ratios; for large gap ratios (up to 0.7), only a upstream movement along the backside of the cylinder is observed. The rear stagnation point moves downstream and then upstream along the backside of the cylinder as the Reynolds number increases at small gap ratios, coinciding with the growth of the upper and lower vortices attached on the backside of the cylinder, respectively. For a gap ratio of 0.7, this point moves upward along the cylinder due to the growth of the lower vortex.

For unsteady flow, the locations of the separation and stagnation points oscillate on the cylinder due to vortex shedding. An increase in the gap ratio leads to an increase in both the oscillation amplitude and the frequency due to the weakening of the wall suppression effect. The oscillation amplitude for the lower separation point is slightly larger than for the upper separation point since a larger flow gap velocity induces a stronger vortex shedding behind the cylinder bottom. This mechanism also leads to larger oscillation amplitudes for both the front stagnation point and the lower separation point at large gap ratios than those for the isolated cylinder. Moreover, the minimum values of the separation and stagnation angles are more affected by the gap ratio than the maximum values due to the stronger interaction with the bottom wall.

ACKNOWLEDGMENTS

We gratefully acknowledge the support for this research from the Department of Marine Technology, Norwegian University of

Science and Technology, and the Norwegian Research Council, Grant No. 308745.

DATA AVAILABILITY

The data that support the findings of this study are available from the corresponding author upon reasonable request.

REFERENCES

- ¹B. Sumer and J. Fredsøe, *Hydrodynamics around Cylindrical Structures* (World Scientific, 2006), Vol. 26.
- ²M. Wu, C. Wen, R. Yen, M. Weng, and A. Wang, “Experimental and numerical study of the separation angle for flow around a circular cylinder at low Reynolds number,” *J. Fluid Mech.* **515**, 233 (2004).
- ³S. Sen, S. Mittal, and G. Biswas, “Steady separated flow past a circular cylinder at low Reynolds numbers,” *J. Fluid Mech.* **620**, 89 (2009).
- ⁴H. Jiang, “Separation angle for flow past a circular cylinder in the subcritical regime,” *Phys. Fluids* **32**, 014106 (2020).
- ⁵W. Huang and H. Sung, “Vortex shedding from a circular cylinder near a moving wall,” *J. Fluids Struct.* **23**, 1064–1076 (2007).
- ⁶H. Jiang, L. Cheng, S. Draper, and H. An, “Two- and three-dimensional instabilities in the wake of a circular cylinder near a moving wall,” *J. Fluid Mech.* **812**, 435–462 (2017).
- ⁷W. Khan, J. Culham, and M. M. Yovanovich, “Fluid flow around and heat transfer from elliptical cylinders: Analytical approach,” *J. Thermophys. Heat Transfer* **19**, 178–185 (2005).
- ⁸B. Jensen, S. Carstensen, and E. Christensen, “Mixing of stratified flow around bridge piers in steady current,” *J. Hydraul. Eng.* **144**, 04018041 (2018).
- ⁹I. Paul, K. Prakash, and S. Vengadesan, “Onset of laminar separation and vortex shedding in flow past unconfined elliptic cylinders,” *Phys. Fluids* **26**, 023601 (2014).

- ¹⁰Z. Faruquee, D. Ting, A. Fartaj, R. Barron, and R. Carriveau, "The effects of axis ratio on laminar fluid flow around an elliptical cylinder," *Int. J. Heat Fluid Flow* **28**, 1178–1189 (2007).
- ¹¹S. Sen, S. Mittal, and G. Biswas, "Steady separated flow past elliptic cylinders using a stabilized finite-element method," *Comput. Model. Eng. Sci.* **86**, 1–28 (2012).
- ¹²J. Zhu, L. Holmedal, D. Myrhaug, and H. Wang, "Near-wall effect on flow around an elliptic cylinder translating above a plane wall," *Phys. Fluids* **32**, 093607 (2020).
- ¹³H. Beem, "Seal whiskers inspire marine technology," *Oceanus Mag.* **51**, 82–85 (2016).
- ¹⁴H. R. Beem and M. S. Triantafyllou, "Wake-induced 'slaloming' response explains exquisite sensitivity of seal whisker-like sensors," *J. Fluid Mech.* **783**, 306–322 (2015).
- ¹⁵I. C. Rust and H. H. Asada, "The eyeball ROV: Design and control of a spherical underwater vehicle steered by an internal eccentric mass," in *IEEE International Conference on Robotics and Automation* (IEEE, 2011), pp. 5855–5862.
- ¹⁶A. Mazumdar, M. Y. Chuah, M. S. Triantafyllou, and H. H. Asada, "Design for precision multi-directional maneuverability: Egg-shaped underwater robots for infrastructure inspection," in *IEEE International Conference on Robotics and Automation (ICRA)* (IEEE, 2014), pp. 2950–2956.
- ¹⁷B. Stewart, M. Thompson, T. Leweke, and K. Hourigan, "The wake behind a cylinder rolling on a wall at varying rotation rates," *J. Fluid Mech.* **648**, 225 (2010).
- ¹⁸H. Takami and H. Keller, "Steady two-dimensional viscous flow of an incompressible fluid past a circular cylinder," *Phys. Fluids* **12**, II-51 (1969).
- ¹⁹S. Dennis and G.-Z. Chang, "Numerical solutions for steady flow past a circular cylinder at Reynolds numbers up to 100," *J. Fluid Mech.* **42**, 471–489 (1970).
- ²⁰Y.-H. Tseng and J. Ferziger, "A ghost-cell immersed boundary method for flow in complex geometry," *J. Comput. Phys.* **192**, 593–623 (2003).
- ²¹P. Berthelsen and O. Faltinsen, "A local directional ghost cell approach for incompressible viscous flow problems with irregular boundaries," *J. Comput. Phys.* **227**, 4354–4397 (2008).
- ²²J. Kim, D. Kim, and H. Choi, "An immersed-boundary finite-volume method for simulations of flow in complex geometries," *J. Comput. Phys.* **171**, 132–150 (2001).
- ²³J. Park, K. Kwon, and H. Choi, "Numerical solutions of flow past a circular cylinder at Reynolds numbers up to 160," *KSME Int. J.* **12**, 1200–1205 (1998).
- ²⁴X. Shi, M. Alam, and H. Bai, "Wakes of elliptical cylinders at low Reynolds number," *Int. J. Heat Fluid Flow* **82**, 108553 (2020).
- ²⁵M. Thompson, A. Radi, A. Rao, J. Sheridan, and K. Hourigan, "Low-Reynolds-number wakes of elliptical cylinders: From the circular cylinder to the normal flat plate," *J. Fluid Mech.* **751**, 570 (2014).
- ²⁶A. Radi, M. C. Thompson, J. Sheridan, and K. Hourigan, "From the circular cylinder to the flat plate wake: The variation of Strouhal number with Reynolds number for elliptical cylinders," *Phys. Fluids* **25**, 101706 (2013).
- ²⁷J. Zhu, F. Jiang, and L. E. Holmedal, "Three-dimensional wake transition behind an elliptic cylinder near a moving wall," *Phys. Fluids* **33**, 043606 (2021).